Unravelling intrusion-induced forced fold kinematics and ground deformation using 3D seismic reflection data

Jennifer Reeves, Craig Magee*, Christopher A-L Jackson
Basins Research Group, Imperial College London, London, SW7 2BP, UK
*corresponding author: c.magee@imperial.ac.uk

ABSTRACT

Sills emplaced at shallow-levels are commonly accommodated by overburden uplift, producing forced folds. We examine ancient forced folds developed above saucer-shaped sills using 3D seismic reflection data from the Canterbury Basin, offshore SE New Zealand. Seismic-stratigraphic relationships indicate sill emplacement occurred incrementally over ~31 Myr between the Oligocene (~35–32 Ma) and Early Pliocene (~5–4 Ma). Two folds display flat-topped geometries and amplitudes that decrease upwards, conforming to expected models of forced fold growth. Conversely, two folds display amplitudes that locally increase upwards, coincident with a transition from flat-topped to dome-shaped morphologies and an across-fold thickening of strata. We suggest these discrepancies between observed and expected forced fold geometry reflect uplift and subsidence cycles driven by sill inflation and deflation. Unravelling these forced fold kinematic histories shows complex intrusion geometries can produce relatively simple ground deformation patterns, with magma transgression corresponds to localisation of uplift.

1 INTRODUCTION

Uplift of Earth's surface in response to shallow-level magma movement provides crucial insights into volcano activity, potentially warning of impending eruptions (e.g., Sturkell et al., 2006; Biggs et al., 2009; Sparks et al., 2012; van Wyk de Vries et al., 2014). Inverting ground deformation patterns recorded at monitored volcanoes to map magma movement is difficult, however, because we cannot directly observe the host rock deformation mechanisms accommodating intrusion or validate models (Galland, 2012). We thus typically assume that ground deformation results from elastic bending of the overburden (i.e. forced folding), such that the area of surface uplift is expected to directly correlate to the location and size of an underlying intrusion (Galland, 2012). Importantly, analyses of forced folds above ancient sills and laccoliths, exposed at Earth's surface or imaged in seismic reflection data, reveal that a combination of elastic bending and inelastic processes (e.g. faulting, fluidisation, and pore collapse) can accommodate emplaced magma (e.g., Pollard and Johnson, 1973; Galland and Scheibert, 2013; Jackson et al., 2013; Magee et al., 2013; van Wyk de Vries et al., 2014). The likely occurrence of inelastic deformation processes implies that traditional inversion of ground deformation data assuming pure elastic bending of the host rock will underestimate magma volumes (e.g., Schofield et al., 2014). It thus remains challenging to compare active and ancient systems because the dynamic deformation processes that cumulatively build a forced fold are difficult to deduce when magmatism has long-since ceased.

Here, we analyse a magma plumbing system imaged in 3D seismic reflection data from the petroliferous Canterbury Basin, offshore SE New Zealand (Fig. 1), and identify four saucer-shaped sills intruded into Cretaceous-to-Eocene strata. The sills are overlain by dome-shaped forced folds and generated hydrothermal vents above their lateral tips. Because intrusion-induced forced folds and hydrothermal vents are expressed as topographic or bathymetric highs at the contemporaneous surface, numerous studies have used the age of overlying strata that onto these structures as a method for determining the timing of magmatism (e.g., Trude et al., 2003; Jamtveit et al., 2004; Hansen and Cartwright, 2006; Magee et al., 2013). Whilst most studies assume that onlap of strata onto the top of forced folds marks the age of instantaneous emplacement (Trude et al., 2003), we show that multiple onlap events can be recognised throughout the folded sedimentary succession. Our analysis of seismic-stratigraphic relationships between the hydrothermal vents, forced folds, and overlying strata reveals three main phases of forced fold growth and thus sill emplacement in the Oligocene (~35–32 Ma), Miocene (~19–16 Ma), and Pliocene (~5–4 Ma); these phases of emplacement indicate magmatism overlapped with and may have impacted petroleum generation, migration, and accumulation. Seismic-stratigraphic onlap onto intrusion-induced forced folds is thus a powerful tool for determining timing of magmatic activity (e.g., Trude et al., 2003), although we demonstrate that we should not solely rely on defining strata onlapping onto the top of forced folds to constrain emplacement age (Magee et al., 2014). Identifying seismic-stratigraphic relationships throughout folded sequences allows forced fold kinematics to be unravelled and we show, for the first time, that intermittent subsidence can play an important role in intrusion-induced forced folding.

2 Geological setting

The Canterbury Basin, located offshore SE New Zealand (Fig. 1), is bound by the Chatham Rise to the north and the Bounty Trough to the south. Basin formation occurred in response to rifting between New Zealand, Antarctica, and Australia in the Late Albian-to-Early Campanian (Fig. 2) (e.g., Fulthorpe et al., 1996; Lu and Fulthorpe, 2004). The basement broadly corresponds to the Torlesse Supergroup, a series of Permian-to-Early Cretaceous greywacke and argillite meta-sedimentary rocks (Uruski, 2010). Graben and half-graben formed during this Middle-Cretaceous phase of rifting were infilled by fluvial and paralic sediments, including coal that forms the main source rock in the region (Fig. 2) (i.e. the Horse Range and Katiki formations; Carter, 1988; Killops et al., 1997; Uruski, 2010). The onset of passive subsidence and a marine transgression in the Late Cretaceous defined the transition to the post-rift period, characterised stratigraphically by the upwards progression from terrestrial sandstone and coal (i.e. the Pukeiwihai Formation) to deposition of marine sandstone, mudstone, and siltstone (Fig. 2) (i.e. the Katiki, Moreaki, and Hampden formations; Carter, 1988; Killops et al., 1997). Some of the Paleogene mudstone represent potential source rocks (Fig. 2) (Bennett et al., 2000). Overlying these formations is the marine Amuri Limestone (Fig. 2) (Fulthorpe et al., 1996). The point of maximum transgression at ~29 Ma is marked in the Canterbury Basin by a regional unconformity (Fig. 2) (e.g., Carter, 1988; Fulthorpe et al., 1996). Continued uplift and an increase in the supply of terrigenous silt and sand drove the eastward progradation of continental shelf and slope deposits in the Early Miocene-to-Recent (Fig. 2) (i.e. the Tokama Siltstone; Lu et al., 2005). Hydrocarbon generation, migration, and accumulation in the Canterbury Basin likely began in the ~Middle Miocene when Middle-to-Late Cretaceous coals were buried to sufficient depths (Fig. 2) (e.g., Bennett et al., 2000). Most plays rely on stratigraphic traps within Upper Cretaceous sandstone reservoirs, although Eocene sandstone reservoirs within Miocene fault- and fold-related structural traps also form viable prospects (Fig. 2) (Bennett et al., 2000).

3 Dataset and methodology

We use a pre-stacked time-migrated (PSTM) 3D seismic reflection survey (Waka) tied to three regional boreholes (i.e. Galleon-1, Endeavour-1, and Cutter-1) by PSTM 2D seismic surveys (Fig. 1). The 3D seismic data cover a ~1428 km^2 area, of which we focus on ~314 km^2 (Fig. 1). Inline (NE–SW) and crossline (NW–SE) spacing is 25 m and 12.5 m, respectively. The data are displayed with a SEG normal polarity, whereby a downward increase in acoustic impedance corresponds to a positive (red) reflection. Within the focused study area, the water depth is 863–1948 ms TWTT (two-way travel time), or 647–1461 m assuming a water velocity of 1480 m s^{-1}. Three, NW-trending submarine canyons are developed at the seabed (Fig. 3A), with seismic reflections directly beneath them being down-warped, decreasing in amplitude with depth, and mirroring the channel plan-view morphology (Fig. 3B). We consider that the apparent expression of the submarine channels within the underlying reflections reflection is a geophysical artefact attributable to velocity push-down, caused by acoustically slow seawater being juxtaposed against shallowly buried, but still acoustically faster sediment/rock.

We use borehole data to define the age and lithology of ten mapped stratigraphic horizons (H1-H10) (Figs 2 and 3); four sills (S1-S4) were also mapped (Fig. 3). All three wells display consistent time-depth relationships, suggesting that the area of interest has a simple velocity structure (Fig. 4). We use a 2nd order polynomial best-fit line to the checkshot data from the three boreholes to broadly define interval velocities for the Seabed–H10 (1800 m s^{-1}), H10–H2 (2800 m s^{-1}), and H2–H1 (3600 m s^{-1}). However, the boreholes are located on the continental shelf where stratigraphy is ~700 ms TWTT shallower than in the area covered by the 3D seismic survey (Fig. 1), implying that these velocities are minimum estimates for those encountered in our study area. We use our simple velocity model to depth convert structural maps and measurements from time to depth. Depth-conversion of the seismic data using the derived velocity was attempted in order to remove the velocity push-down artefacts, which hinder our geometric interpretation of the seismically imaged geology. Whilst we were unable to fully remove the imprint of the velocity push-downs, which suggests our simple model utilised does not fully capture the true velocity structure of the study area, the depth-conversion significantly reduced their imaging impact and, thereby, facilitated greater confidence in structural interpretations (Fig. 3B). Using our simple velocity model we created depth-structure and isopach maps for and between key stratigraphic horizons, respectively, thereby highlighting lateral variations in stratal thickness that may be related to tectonics and magmatism.

A dominant frequency that decreases downwards from ~35 Hz to 25 Hz within the interval of interest, coupled with the inferred velocity structure, suggests that the limit of separability within the data increases with depth from 13 m to 36 m; we calculate the limit of visibility to increase from 2 m to 5 m (Brown, 2004). Assuming an interval velocity of 5550 m s^{-1} for the mapped intrusions (Skogly, 1998) and taking the local dominant frequency of ~25 Hz, we estimate that the limits of separability and visibility are 55 m and 7 m, respectively. Sills between 7–56 m thick will therefore be expressed in seismic data as tuned reflection packages, i.e. where reflections from the top and base intrusion contacts constructively interfere and cannot be distinguished, meaning we cannot calculate true sill thickness.

4 RESULTS

4.1 Sills

We mapped four, broadly saucer-shaped sills (S1–S4), which are expressed as packages of high-amplitude reflections, consisting of a strata-concordant inner sill encompassed by an inclined, transgressive limb (Figs 3 and 5-7). The base of S1 is located immediately below H2, although there is a south-dipping inclined sheet that extends from S1 down to the basement-cover interface (H1) (Figs 3, 6A, and C). The basal strata-concordant sections of S2–S4 typically coincide with H1 (Figs 3 and 7). S1 and S2 are elongated ENE-WSW and ESE-WSW and their long axes and plan-view aspect ratios are 6.3 km and 7.5 km, and 1.5 and 1.7, respectively; the inner sill length of both S1 and S2 is 4.5 km (Fig. 5). In detail, S3 consists of several saucer-like depressions bound by transgressive inclined limbs, which become shallower towards the NE, below Fold 3 (Figs 5 and 7A). S4 occurs between S1 and S2, displays a rather irregular inner sill morphology, and shallows to the NE (Fig. 5). S3 and S4 extend beyond the limits of the 3D seismic survey, thus we cannot determine their true dimension. However, their long axes are a minimum of 9.1 km (S3) and 14.5 km (S4) (Fig. 5).

4.2 Supra-sill structure

The top of the basement (H1) in the study area is dominated by a NE-trending, ~29 km long, ~0.5 km high ridge along its south-eastern boundary, but also displays a series of smaller, variably shaped structural highs (Fig. 8). Overlying strata onlap the basement (H1) and dip gently eastward (Fig. 3B). Superimposed onto the regional structure of H2–H8 are three, prominent elliptical folds (i.e. folds 1-3) that have long axes of 6.2 km, 6.4 km, and 4.6 km respectively (Fig. 8). The true geometry of Fold 3 is difficult to ascertain because its south-eastern limit appears to coincide with an area of velocity push-downs related to seabed submarine canyons (Figs 3B and 8). We also observe a broad, 11 km long elliptical dome is also observed between H2–H8 (i.e. Fold 4; Fig. 8). The outlines of folds 1-2 overlie the lateral terminations of S1 and S2, respectively, Fold 3 overlies a relatively shallow portion of S3, and the central part of Fold 4 is underlain by S4 (Fig. 5).

4.2.1 Fold geometries between H2–H8

Between H2–H8, folds 1 and 2 have relatively flat-tops, parallel to the regional structural dip of the host sedimentary sequence, and are bound by monoclines (Figs 3 and 6-8). At lower stratigraphic levels (e.g. H3 and H5), the centre of Fold 1 appears to be depressed relative to its margins (Fig. 8). Low-throw (<50 m) reverse faults coincident with and extending up to H8 above the S1 inclined limbs, offset the Fold 1 monoclines around ~9 km of the ~14 km fold circumference (Figs 5 and 6). Above the inclined limbs of S2, three laterally restricted (~0.9–1.8 km long), low-throw (<50 m) reverse faults offset the Fold 2 monoclines within the H3–

H7 sequence (Figs 3B and 5). The maximum amplitudes at H3 for the two folds are ~51 m (Fold 1) and ~54 m (Fold 2), whereas maximum amplitudes at H8 are 59 m (Fold 1) and 78 m (Fold 2) (Figs 6, 7A, and 8). Compared to folds 1 and 2, Fold 3 has a more rounded top and has a maximum amplitude of 110 m at H8 (Figs 7B and 8). The amplitude of Fold 4 decreases upwards, from 103 m at H7 to 58 m at H8 (Figs 3 and 8). Relative to regional stratal thickness patterns, we observe minor variations in H2–H8 thickness across folds 1-3, whereas a prominent thinning is observed across Fold 4 (Fig. 9).

4.2.2 Fold geometries between H8–H10

Within Fold 1 and between H8–H10 (i.e. the fold top), we observe numerous seismic stratigraphic onlap and truncation relationships at various structural levels, particularly onto H8, H9, and H10 (Fig. 6). From H8 to H10, there is a gradual transition in the morphology of Fold 1 from flat-topped to dome-shaped, which corresponds to an increase in fold amplitude from 59 m at H8, to 120 m at H9, and 90 m at H10 (Figs 3B, 6, and 8). This change in Fold 1 morphology occurs between H8–H9, where the thickness of this stratal package increases from ~230 m beyond the immediate fold periphery up to ~303 m across the fold crest (Fig. 9). There are several reflections between H8–H9, which apparently downlap onto underlying reflections and only occur within the limits of Fold 1 (Fig. 6).

Fold 2 displays onlap and truncation patterns from just below H8 to H10, where it has a maximum amplitude of 64 m, but its geometry remains flat-topped and the H8–H10 strata thin across the fold (Figs 7A, 8, and 9). Onlap and truncation patterns are also observed in Fold 3 between H7 and H9 (i.e. the top of the fold), where it has an amplitude of 125 m (Fig. 7B). We only observe onlap onto the top of Fold 4 at H8 (Fig. 3B). Folds 1-3 are, in places, incised by presumably deep-marine channels (e.g., Figs 3 and 7B).

4.3 Mound-like structures

Associated with folds 1 and 2 are a series of craters, dome-, and eye-shaped mounds that truncate and/or downlap onto various stratigraphic horizons between H8–H10, and are onlapped by overlying strata (e.g., Figs 7A and 10). These mounds have diameters and heights of ~200–500 m and ~30–80 m, respectively (e.g., Figs 7A and 10). All mounds are located at the fold peripheries and underlain by a zone of low-amplitude, chaotic reflections that extends down to lateral sill terminations (e.g., Fig. 10).

Figure 10: (A) Root mean squared (RMS) amplitude map of H8 over S1. Warm colours correspond to areas of high amplitude, whereas cold colours are areas of low amplitude. Hydrothermal vent conduits are highlighted by the red circles. (B) Interpreted seismic section showing a hydrothermal vent, onlapped by overlying strata, and underlain by a pipe-like zone of disturbed reflections. See Figure 8A for location.

5 Discussion

5.1 Magma emplacement

Space to accommodate magma intrusion is commonly generated by deformation of the host rock. At shallow-levels in sedimentary basins, intrusions often develop sill-like geometries as magma is emplaced along mechanical contrasts between layered strata, weak sedimentary rocks, and/or the minimum principal stress axis rotates to vertical (e.g., Kavanagh et al., 2006; Gudmundsson, 2011; Schofield et al., 2012; Magee et al., 2016; Walker et al., 2017). As intrusion continues and the sill inflates, space can be generated by uplift of the overburden and free surface to form dome-shaped forced folds (e.g., Pollard and Johnson, 1973; Hansen and Cartwright, 2006); ground deformation driven by intrusion-induced forced folding is akin to the uplift observed at active volcanoes generated by magma movement and accumulation (e.g., Castro et al., 2016; Magee et al., 2017a). Given the broad spatial coincidence between fold outlines and sill terminations (e.g., Figs 3 and 5-7), we suggest that folds 1-3 formed in response to the intrusion of S1-S3, respectively (Stearns, 1978; Hansen and Cartwright, 2006). This forced fold interpretation is supported by evidence of onlap onto folds 1-3 at various stratigraphic levels (Figs 3, 6, and 7), which indicates that the domes had a bathymetric expression (e.g., Trude et al., 2003; Hansen and Cartwright, 2006). S4 is broadly overlain by a dome-shaped fold, which is onlapped at H8 by overlying strata, but the fold extends beyond the limit of the sill to the SE by up to ~6 km (Fig. 5). We suggest that part of Fold 4 was generated in response to sill emplacement but has interfered and merged with a differential compaction fold developed over the NE-SW oriented basement high (Figs 3, 5, and 8).

5.1.1 Timing of sill intrusion and tectono-magmatic context

Identification of onlapping reflections onto numerous stratigraphic horizons between H8–H10 and H7–H9 within folds 1-2 and Fold 3, respectively, indicate that sill emplacement instigated doming of the palaeo-seabed for a prolonged period of time (Figs 3, 6, and 7). Similarly, the mound-like structures, which are reminiscent of and interpreted to be hydrothermal vents, occur at various stratigraphic levels between H8–H10 and are onlapped by overlying strata (e.g., Fig. 10) (e.g., Jamtveit et al., 2004; Hansen, 2006). We recognise four main phases of intrusion, based on prominent seismic-stratigraphic onlap and truncation relationships at H7 for Fold 3, H8 for folds 1-4, H9 for folds 1 and 3, and H10 for folds 1 and 2 (Figs 3, 6, and 7). Biostratigraphic dating of these sedimentary horizons within the interval of interest indicates that sill emplacement principally occurred in the Oligocene (i.e. H7–H8, ~35–32 Ma), the Early Miocene (i.e. H9, ~19–16 Ma), and the Early Pliocene (i.e. H10, ~5–4 Ma) (Fig. 2). The occurrence of subtle onlap and truncation observed within folded strata deposited between these principal phases of magmatism implies that sill emplacement occurred intermittently over ~31 Myr (Figs 3, 6, and 7), consistent with previous observations that sill-complexes can assemble incrementally across protracted periods of time (Magee et al., 2014; Magee et al., 2017a). We suggest that magma ascending in the Early Miocene and Early Pliocene, after the initial emplacement of S1–S3, likely became trapped along the contact of the pre-existing sills and therefore reactivated the growth of the forced folds.

The Oligocene (35–32 Ma) initial emplacement of S1–S3 was concurrent with the Waiareka-Deborah volcanics and/or the Cookson volcanics (Fig. 2) (Timm et al., 2010). This magmatic event coincides with and may be genetically related to the opening and separation of Australia and Antarctica, which occurred ~33–30 Ma (e.g., Jenkins, 1974), and/or the northwards propagation of the Emerald Basin spreading zone (Uruski, 2010). Sill emplacement during the Early Miocene (~19–16 Ma) likely correlates to either the onshore development of the 27–12 Ma Oxford Volcanics in Central Canterbury or the 16–11 Ma Dunedin Volcano on the Otago Peninsula, which is located only ~50 km to the WSW of the study area (Fig. 2). It is difficult to link Early Pliocene sill emplacement (5–4 Ma) to other magmatic events that occurred in and around the Canterbury Basin, although it may relate the ~2.6 Myr old basaltic Geraldine and Timaru lavas (Timm et al., 2010).

5.1.2 Fold amplitude as a proxy for sill thickness

Assuming that shallow-level sill emplacement is fully accommodated by elastic bending of the overburden implies that the amplitude of a forced fold is equivalent to the thickness of the forcing intrusion (Fig. 11A) (e.g., Pollard and Johnson, 1973; Goulty and Schofield, 2008; Jackson et al., 2013). Inversion of ground deformation data collected from active volcanoes and related to subsurface magma movement also typically assumes that host rock deformation occurs via elastic bending, such that the size and location of the surface uplift and/or subsidence is expected to broadly reflect the volume and position of the magma body (e.g., Biggs et al., 2011; Galland, 2012; Pagli et al., 2012). If space for magma emplacement is also generated by the contemporaneous occurrence of inelastic host rock deformation processes (e.g., fluidisation and porosity reduction), fold amplitude will be less than the thickness of the intrusion (e.g., Jackson et al., 2013; Magee et al., 2013; Magee et al., 2017b).

The sills imaged in seismic reflection data here are expressed as tuned reflection packages and are therefore probably <56 m thick, assuming the intrusions have an interval velocity of 5550 m s^{-1}. However, all maximum fold amplitudes measured at identified fold tops are ≥59 m and up to 125 m (i.e. Fold 3 at H9); if sill thickness is at the limit of detectability (i.e. 7 m), differences between fold amplitude and sill thickness could thus be up to ~120 m. These unexpected discrepancies where fold amplitude is greater than sill thickness could be because: (i) the sills have a faster seismic velocity than 5550 m s^{-1}, which would increase the limit of separability (e.g., an interval velocity of 7000 m s^{-1} would mean the sills could be up to 70 m thick); (ii) seismic velocity of the sedimentary sequence is overestimated, meaning that depth-converted fold amplitudes are accentuated, although we note that the increased depth of the study area relative to the boreholes implies the velocities used are minimum end-members; and/or (iii) multiple, seismically undetectable sills (i.e. <7 m thick) contributed to fold generation.

In addition to the discrepancy between maximum forced fold amplitude and sill thickness, our observations reveal that amplitude varies with stratigraphic level. For example, Fold 4 has an amplitude of 103 m at H7 but 58 m at H8 (i.e. the top of the fold) (Fig. 3B). Because Fold 4 is only onlapped at H8 (Fig. 3B), suggesting it formed in a single intrusion event, the upwards decay in fold amplitude may relate to a syn-kinematic increase in ductile strain and inelastic deformation (e.g., compaction) towards the top of the fold (e.g., Pollard and Johnson, 1973; Hansen and Cartwright, 2006). Fold 2 also decreases in amplitude upwards, from 78 m at H8 to 64 m at H10 (Figs 7A and 8), but developed across multiple intrusion events. The upper portions of Fold 2, between H8–H10 are thus expected to have been superimposed and added onto the original forced fold generated in the Oligocene. For Fold 2, the formation of a 64 m high fold during the Early Pliocene implies that the Oligocene fold had an original amplitude of 14 m.

In contrast to folds 2 and 4, the amplitude of folds 1 and 3 increases with stratigraphic height; i.e. Fold 1 increases in amplitude from 59 m at H8 to 120 m at H9, decreasing to 90 m at H10, whereas Fold 3 has an amplitude of 110 m at H8 but 125 m at H9 (Figs 6, 7B, and 8). These increases in amplitude are associated with a change in fold geometry from flat-topped to dome-shaped and a subtle increase thickness of the H8–H9 sequence across folds 1 and 3 (Figs 6, 7B, 8, and 9). Within Fold 1, where the change in fold style from H8 to H9 is more prominent, the increased amount of reflections within the fold and presence of seismic-stratigraphic onlap and apparent downlap (i.e. rotated onlaps) suggest that there are several, thin packages of material that only occur across the fold crest (Fig. 6). These additional rock packages, which are restricted to the fold, accommodate the observed increase in amplitude and H8–H9 thickness (Fig. 6). It is important to note that these increases in amplitude and thickness, a change in fold morphology (i.e. from flat-topped to dome-shaped), and occurrence of additional material solely within the folded sequence contrasts with our conceptual model of intrusion-induced forced folding (Fig. 11A) (cf. Pollard and Johnson, 1973; Hansen and Cartwright, 2006; Galland, 2012; Magee et al., 2014). For example, because the geometry and growth of forced folds are controlled by a directly underlying forcing member, it is expected that whatever happens to the upper layers within a forced fold must also happen to the lower layers (Fig. 11A) (Stearns, 1978).

We suggest that the protracted development of Fold 1, and to a lesser extent Fold 3, involved repeated episodes of uplift and subsidence related to several discrete periods of sill injection and evacuation (Fig. 11B). In particular, we envisage that the intrusion and inflation of tabular sills uplifted the overburden to form flat-topped folds, which were expressed at the palaeosurface and became onlapped by depositing sediment (Fig. 11B). It is likely that Fold 1 formation was facilitated by circumferential reverse faulting and elastic bending (Figs 5, 6, and 10B). With continued inflation and bending of the overburden, eventual tensile fracturing of the host rock immediately overlying the lateral terminations of the tabular sill allows magma to transgress upwards and form the inclined limbs of a widening saucer-shaped sill (Fig. 11B). Exploitation of reverse faults by magma may also promote inclined limb development (Figs 6 and 11B). If the melt supply to the entire sill wanes during the emplacement of the inclined limbs, their propagation will be fed by magma evacuating from the inner, tabular sill (Fig. 11B). This redistribution of magma will maintain or enhance the original flat-topped fold around its rim but promote subsidence of the fold crest, which may be infilled by depositing sediment, as the underlying inner sill thins (Fig. 11B). Where a later injection of magma into the inner sill or along its contact re-inflates the forced fold, the strata deposited within the folded sequence will rotate and appear to downlap onto the underlying surface, producing a more dome-shaped fold geometry (Figs 6, 8, and 11B). Repeated periods of sill injection and evacuation into the inclined limbs over a protracted period of time could explain the observed increase in fold amplitude and stratal thickness, as well as the occurrence of fold-restricted reflections, as observed in folds 1 and 3 between H8–H9 (Figs 6, 7B, 8, 9, and 11B). Similar uplift and subsidence patterns have been observed to affect forced folds at active volcanoes, albeit on a much smaller spatial and temporal scale (Pagli et al., 2012; Magee et al., 2017a).

Alternatively, the injection of multiple, seismically undetectable, thin sills (i.e. <5 m thick) into the H8–H10 succession could produce the observed fold geometries (Fig. 11C); this model could, to some extent, also explain the seismic-stratigraphic relationships if emplacement occurred incrementally. However, for Fold 1, a cumulative sill thickness of 59 m is required to increase the fold amplitude of 59 m at H8 to 120 m at H9. Whilst borehole from the Faroe-Shetland Basins suggest that a significant proportion of sills may not be resolved or detected in seismic reflection data (Schofield et al., 2017), perhaps supporting the thin sill model, a recent study has proposed that the high acoustic impedance contrast between igneous and sedimentary rocks means that even very thin sills should be detected in seismic data (Eide et al., 2017). We thus consider it unlikely that multiple, thin sills (<5 m thick) occur within the H8–H9 folded sequence of folds 1 and 3.

5.2 Implications for using seismic reflection data to inform interpretation of ground deformation at active volcanoes

Reflection seismology is the only technique that allows the entire 3D geometry of natural, shallow-level intrusions and associated host rock structures to be visualised and quantified at a relatively high-resolution (e.g., Smallwood and Maresh, 2002; Hansen and Cartwright, 2006; Magee et al., 2016). Seismic reflection data thus provides a unique opportunity to investigate how overburden uplift (i.e. forced folding) and subsidence accommodates intrusions and is expressed at the contemporaneous surface (e.g., Trude et al., 2003; Hansen and Cartwright, 2006; Jackson et al., 2013). For example, discrepancies between fold amplitudes and intrusion thicknesses measured in seismic reflection data, coupled with field observations, have highlighted that inelastic deformation processes can play an important role in accommodating magma volumes (e.g., Jackson et al., 2013; Magee et al., 2013). To date, however, the vast majority of seismic-based studies examining intrusion-induced forced folds adopt an interpretation framework that assumes magma emplacement and fold growth occurred instantaneously (e.g., Trude et al., 2003; Hansen and Cartwright, 2006; Jackson et al., 2013). Whilst this instantaneous model may be appropriate for forced folds developed during single, short-lived magma injection events, observations of active emplacement and host rock deformation from field-, geophysical-, and geodetic-based studies reveal that forced folds can evolve through multiple uplift and subsidence episodes (e.g., Sturkell et al., 2006; Magee et al., 2017a). It is thus difficult to reconcile insights into the processes controlling ground deformation obtained from seismic reflection data, which only provide a snapshot of the cumulative strain accommodating ancient intrusions, and the dynamic uplift and subsidence recorded at active volcanoes. We show that mapping of intra-fold strata and identification of seismic-stratigraphic relationships can be used to unravel the incremental development of sill intrusions and overlying forced folds (see also Magee et al., 2014). Furthermore, our results provide the first evidence from seismic reflection data that the dynamic interplay between uplift and subsidence can control forced fold geometries. We suggest that broad areas of uplift likely correspond to the inflation of magma reservoirs, whereas the transition to broad subsidence and localised uplift (e.g., above inclined limbs of saucer-shaped sills) marks the onset of magma transgression. Importantly, our observations also emphasise that relatively simple, transient uplift and subsidence patterns can be produced by complex intrusion morphologies (Galland, 2012; Magee et al., 2017a).

5.3 Implications for hydrocarbon exploration

Deciphering how the host rock deforms and accommodates the intruded magma volume is also important from a hydrocarbon exploration perspective because: (i) elastic folding of the overburden and free surface above intruding, shallow-level (< 2 km depth) sills can produce forced folds that may result in the formation of structural (i.e. four-way dip closures) and stratigraphic (i.e. pinchout) traps (e.g., Reeckmann and Mebberson, 1984; Smallwood and Maresh, 2002; Schutter, 2003; Schmiedel et al., 2017); (ii) intrusion-induced faulting and fracturing, which may accompany folding, can increase local permeability and potentially breach traps or compartmentalise reservoirs (e.g., Reeckmann and Mebberson, 1984; Holford et al., 2012; Holford et al., 2013); and (iii) inelastic deformation processes involving porosity reduction (e.g., compaction and fluidization) can inhibit hydrocarbon migration and reduce reservoir quality (Schofield et al., 2017). Sill emplacement in the petroliferous Canterbury

Basin throughout the Oligocene-to-Early Pliocene overlapped with the onset of hydrocarbon generation and expulsion in the mid-Miocene (Fig. 2) (Bennett et al., 2000). The sills are spatially restricted and therefore likely to only influence any active petroleum system on a local scale. Sills intrude Cretaceous-to-Palaeogene strata, where the principal source rocks (e.g., coals) are expected (Figs 2, 3, and 6). The imaged sills are probably <55m thick but their impact on source rock maturity is unknown; e.g., sill intrusion could mature or overmature any surrounding source rocks (e.g., Rodriguez Monreal et al., 2009; Holford et al., 2013). Furthermore, it is probable that igneous bodies below the resolution of the seismic data are present and could impact maturation dynamics (Schofield et al., 2017). The forced folds deform potential Late Cretaceous and Eocene reservoir rocks, creating possible structural traps (Figs 2, 3, and 6). Other potential traps associated with the forced folds are created by the onlap of strata onto the domes (Fig. 6) (Smallwood and Maresh, 2002; Magee et al., 2017b). Overall, whilst it is difficult to assess whether sill emplacement had a beneficial or adverse effect on petroleum system development, our study highlights that it is critical to not only elucidate magma emplacement mechanics, but also to determine the timing of magmatism relative to hydrocarbon generation and migration.

6 Conclusions

Emplacement of shallow-level sills in sedimentary basins is commonly accommodated by overburden uplift to produce a forced fold that is expressed at the contemporaneous surface. The geometry and kinematics of these intrusion-induced forced folds reflects sill emplacement processes and thus sheds light on how ground deformation relates to magma movement at active volcanoes. Here, we use 3D seismic reflection data from the Canterbury Basin, offshore SE New Zealand, to analyse the timing and formation of four saucer-shaped sill and forced fold pairs. Seismic-stratigraphic onlap and truncation relationships reveal that sill emplacement initially occurred in the Oligocene (~35–22 Ma), followed by two other major intrusive phases in the Early Miocene (~19–16 Ma) and Early Pliocene (~5–4 Ma); these observations indicate that we should not rely on simply identifying onlap relationships at the top of forced folds to assess the age of sill emplacement. Evidence of forced fold growth between these main magmatic events indicates that sill emplacement occurred incrementally over a protracted timespan (~31 Myr). Whilst two of the forced folds conform to the traditional conceptual models of forced fold growth, i.e. fold amplitude decreases up and away from the underlying forcing body, two folds exhibit an upward increase in fold amplitude and a change in morphology from flat-topped to dome-shaped. These changes in fold geometry correspond to the occurrence of additional seismic reflections across and restricted to the fold crests, which locally thicken the folded sequence. We suggest that this unexpected increase in fold amplitude and thickening of strata can be attributed to either: (i) repeated episodes of sill injection and inflation followed by magma evacuation into the inclined limbs of the saucer-shaped, which promoted fold subsidence and locally accommodated deposition of sediments restricted to the deformed sequence; or (ii) the emplacement of seismically undetectable, thin sills within the folded sequence. Furthermore, by unravelling forced fold kinematics, we demonstrate that sill emplacement spanned the generation, migration, and accumulation of hydrocarbons, potentially influencing local petroleum system development. Our observations show that changes in ground deformation patterns, specifically the localisation of uplift and onset of broad subsidence, may indicate magma transgression. Overall, our study shows that analysing structural and stratigraphic relationships across the entire height of a forced fold can provide critical insight into the long-term and dynamic evolution of sill emplacement and associated ground deformation.

ACKNOWLEDGEMENTS

CM is sponsored by an Imperial College Research Fellowship. We are grateful to New Zealand Petroleum and Minerals for data provision and Schlumberger for seismic interpretation software. We also thank numerous colleagues who attended the AAPG Geosciences Technology Workshop on 'Influence of Volcanism and Associated Magmatic Processes on Petroleum Systems' and John Cosgrove for their helpful insights into this work.

Data availability

All seismic and borehole data is freely available from New Zealand Petroleum and Minerals (https://www.nzpam.govt.nz/).

Figure captions

Figure 1: Location map of the study and available seismic reflection and borehole data used.

Figure 2: Tectono-stratigraphic framework of the Canterbury Basin highlighting ages of onshore magmatic events and phases of petroleum system development (after Carter, 1988; Fulthorpe et al., 1996; Killops et al., 1997; Bennett et al., 2000; Timm et al., 2010; Uruski, 2010).

Figure 3: (A) Structure map of the seabed in the study area highlighting the presence of three, deep seafloor canyons. (B) Time-migrated and depth-converted seismic sections showing the effect of velocity push-downs related to the seafloor canyons and the four sills and forced folds studied. Depth-converted seismic sections with vertical exaggeration (VE), to better highlight the fold geometries, and without are shown for comparison. See Figures 1 and 3A for location.

Figure 4: Two-way travel time versus depth curve for the Galleon-1, Cutter-1, and Endeavour-1 boreholes.

Figure 5: Depth-structure map of S1–S4 highlighting the location of reverse faults around sill edges and the position folds 1-4.

Figure 6: Seismic sections and line interpretations through S1 and Fold 1 (A). See Figure 5 for locations.

Figure 7: Seismic sections and line interpretations through S2 and Fold 2 (A), and S3 and Fold 3 (B). See Figure 5 for locations.

Figure 8: Depth-structure maps for H1, H3, H5, H8, and H10.

Figure 9: Thickness (Thick.) maps for intervals H2–H8, H8–H9, and H9–H10.

Figure 10: (A) Root mean squared (RMS) amplitude map of H8 over S1. Warm colours correspond to areas of high amplitude, whereas cold colours are areas of low amplitude. Hydrothermal vent conduits are highlighted by the red circles. (B) Interpreted seismic section showing a hydrothermal vent, onlapped by overlying strata, and underlain by a pipe-like zone of disturbed reflections. See Figure 8A for location.

Figure 11: (A) Schematic summarising the expected fold geometry and onlap relationships for forced folds, specifically folds 1 and 3. (B) Schematic describing how evacuation of a tabular and formation of inclined limbs can drive subsidence across the crest of a forced fold, which can accommodate depositing sediments. Repeated sill inflation/deflation and forced fold uplift/subsidence could produce the observed upward increase in fold amplitude from H8 to H9 and thickening of the H8–H9 strata across the fold. (C) Schematic showing how the

occurrence of seismically undetected, thin sills within the fold could produce the observed upward increase in fold amplitude from H8 to H9 and thickening of the H8–H9 strata across the fold.

References

Bennett, D., Brand, R., Francis, D., Langdale, S., Mills, C., Morris, B., & Tian, X. (2000). *Preliminary results of exploration in the onshore Canterbury Basin.* Paper presented at the 2000 New Zealand Petroleum Exploration Conference Proceedings.

Biggs, J., Anthony, E., & Ebinger, C. (2009). Multiple inflation and deflation events at Kenyan volcanoes, East African Rift. *Geology, 37*(11), 979-982. https://doi.org/10.1130/G30133A.1

Biggs, J., Bastow, I. D., Keir, D., & Lewi, E. (2011). Pulses of deformation reveal frequently recurring shallow magmatic activity beneath the Main Ethiopian Rift. *Geochemistry, Geophysics, Geosystems, 12*(9), Q0AB10. http://dx.doi.org/doi: 10.1029/2011GC003662

Brown, A. R. (2004). *Interpretation of three-dimensional seismic data* (6th ed. Vol. 42). Oklahoma, USA: AAPG and SEG.

Carter, R. (1988). Post-breakup stratigraphy of the Kaikoura Synthem (Cretaceous-Cenozoic), continental margin, southeastern New Zealand. *New Zealand journal of geology and geophysics, 31*(4), 405-429. http://dx.doi.org/10.1080/00288306.1988.10422141

Castro, J. M., Cordonnier, B., Schipper, C. I., Tuffen, H., Baumann, T. S., & Feisel, Y. (2016). Rapid laccolith intrusion driven by explosive volcanic eruption. *Nature communications, 7*, 13585. http://dx.doi.org/10.1038/ncomms13585

Eide, C. H., Schofield, N., Lecomte, I., Buckley, S. J., & Howell, J. A. (2017). Seismic Interpretation of Sill-complexes in Sedimentary Basins: The ‘sub-sill Imaging Problem’. *Journal of the Geological Society of London*

Fulthorpe, C. S., Carter, R. M., Miller, K. G., & Wilson, J. (1996). Marshall Paraconformity: a mid-Oligocene record of inception of the Antarctic circumpolar current and coeval glacio-eustatic lowstand? *Marine and petroleum geology, 13*(1), 61-77. https://doi.org/10.1016/0264-8172(95)00033-X

Galland, O. (2012). Experimental modelling of ground deformation associated with shallow magma intrusions. *Earth and Planetary Science Letters, 317*, 145-156. https://doi.org/10.1016/j.epsl.2011.10.017

Galland, O., & Scheibert, J. (2013). Analytical model of surface uplift above axisymmetric flat-lying magma intrusions: Implications for sill emplacement and geodesy. *Journal of Volcanology and Geothermal Research, 253*, 114-130.

Goulty, N. R., & Schofield, N. (2008). Implications of simple flexure theory for the formation of saucer-shaped sills. *Journal of Structural Geology, 30*(7), 812-817. https://doi.org/10.1016/j.jvolgeores.2012.12.006

Gudmundsson, A. (2011). Deflection of dykes into sills at discontinuities and magma-chamber formation. *Tectonophysics, 500*(1-4), 50-64. https://doi.org/10.1016/j.tecto.2009.10.015

Hansen, D. M. (2006). The morphology of intrusion-related vent structures and their implications for constraining the timing of intrusive events along the NE Atlantic margin. *Journal of the Geological Society of London, 163*, 789-800. https://doi.org/10.1144/0016-76492004-167

Hansen, D. M., & Cartwright, J. (2006). The three-dimensional geometry and growth of forced folds above saucer-shaped igneous sills. *Journal of Structural Geology, 28*(8), 1520-1535. https://doi.org/10.1016/j.jsg.2006.04.004

Holford, S. P., Schofield, N., MacDonald, J. D., Duddy, I. R., & Green, P. F. (2012). Seismic analysis of igneous systems in sedimentary basins and their impacts on hydrocarbon prospectivity: examples from the southern Australian margin. *APPEA Journal*, *52*, 23. https://doi.org/10.1071/AJ11017

Holford, S. P., Schofield, N., Jackson, C. A. L., Magee, C., Green, P. F., & Duddy, I. R. (2013). Impacts of igneous intrusions on source and reservoir potential in prospective sedimentary basins along the western Australian continental margin. In M. Keep & S. J. Moss (Eds.), *The Sedimentary Basins of Western Australia IV*. Perth, WA: Proceedings of the Petroleum Exploration Society of Australia Symposium.

Jackson, C. A.-L., Schofield, N., & Golenkov, B. (2013). Geometry and controls on the development of igneous sill–related forced folds: A 2-D seismic reflection case study from offshore southern Australia. *Geological Society of America Bulletin, 125*(11-12), 1874-1890. https://doi.org/10.1130/B30833.1

Jamtveit, B., Svensen, H., Podladchikov, Y. Y., & Planke, S. (2004). Hydrothermal vent complexes associated with sill intrusions in sedimentary basins. *Physical geology of high-level magmatic systems*, *234*, 233-241.

Jenkins, D. G. (1974). Initiation of the proto circum-Antarctic current. *Nature, 252*(5482), 371-373. https://doi.org/10.1038/252371a0

Kavanagh, J. L., Menand, T., & Sparks, R. S. J. (2006). An experimental investigation of sill formation and propagation in layered elastic media. *Earth and Planetary Science Letters, 245*(3-4), 799-813. https://doi.org/10.1016/j.epsl.2006.03.025

Killops, S., Cook, R., Sykes, R., & Boudou, J. (1997). Petroleum potential and oil-source correlation in the Great South and Canterbury Basins. *New Zealand journal of geology and geophysics, 40*(4), 405-423. http://dx.doi.org/10.1080/00288306.1997.9514773

Lu, H., & Fulthorpe, C. S. (2004). Controls on sequence stratigraphy of a middle Miocene–Holocene, current-swept, passive margin: Offshore Canterbury Basin, New Zealand. *Geological Society of America Bulletin, 116*(11-12), 1345-1366. https://doi.org/10.1130/B2525401.1

Lu, H., Fulthorpe, C. S., Mann, P., & Kominz, M. A. (2005). Miocene–Recent tectonic and climatic controls on sediment supply and sequence stratigraphy: Canterbury basin, New Zealand. *Basin Research, 17*(2), 311-328. http://dx.doi.org/10.1111/j.1365-2117.2005.00266.x

Magee, C., Briggs, F., & Jackson, C. A.-L. (2013). Lithological controls on igneous intrusion-induced ground deformation. *Journal of the Geological Society of London, 170*(6), 853-856. https://doi.org/10.1144/jgs2013-029

Magee, C., Jackson, C. L., & Schofield, N. (2014). Diachronous sub-volcanic intrusion along deep-water margins: insights from the Irish Rockall Basin. *Basin Research, 26*(1), 85-105. http://dx.doi.org/10.1111/bre.12044

Magee, C., Muirhead, J. D., Karvelas, A., Holford, S. P., Jackson, C. A., Bastow, I. D., . . . McCarthy, W. (2016). Lateral magma flow in mafic sill complexes. *Geosphere*, GES01256. 01251. https://doi.org/10.1130/GES01256.1

Magee, C., Bastow, I. D., de Vries, B. v. W., Jackson, C. A.-L., Hetherington, R., Hagos, M., & Hoggett, M. (2017a). Structure and dynamics of surface uplift induced by incremental sill emplacement. *Geology, 45*(5), 431-434. https://doi.org/10.1130/G38839.1

Magee, C., Jackson, C. A.-L., Hardman, J. P., & Reeve, M. T. (2017b). Decoding sill emplacement and forced fold growth in the Exmouth Sub-basin, offshore northwest Australia: Implications for hydrocarbon exploration. *Interpretation, 5*(3), SK11-SK22. https://doi.org/10.1190/INT-2016-0133.1

Pagli, C., Wright, T. J., Ebinger, C. J., Yun, S.-H., Cann, J. R., Barnie, T., & Ayele, A. (2012). Shallow axial magma chamber at the slow-spreading Erta Ale Ridge. *Nature Geoscience, 5*(4), 284-288. https://doi.org/10.1038/ngeo1414

Pollard, D. D., & Johnson, A. M. (1973). Mechanics of growth of some laccolithic intrusions in the Henry Mountains, Utah, II: bending and failure of overburden layers and sill formation. *Tectonophysics, 18*(3), 311-354. https://doi.org/10.1016/0040-1951(73)90051-6

Reeckmann, S. A., & Mebberson, A. J. (1984). Igneous intrusions in the North-West Canning Basin and their impact on oil exploration. In P. G. Purcell (Ed.), *The Canning Basin, WA* (pp. 389-399). Perth, WA: Proceedings of the Geological Society of Australia/Petroleum Exploration Society of Australia Canning Basin Symposium.

Rodriguez Monreal, F., Villar, H., Baudino, R., Delpino, D., & Zencich, S. (2009). Modeling an atypical petroleum system: a case study of hydrocarbon generation, migration and accumulation related to igneous intrusions in the Neuquen Basin, Argentina. *Marine and petroleum geology, 26*(4), 590-605. https://doi.org/10.1016/j.marpetgeo.2009.01.005

Schmiedel, T., Kjoberg, S., Planke, S., Magee, C., Galland, O., Schofield, N., . . . Jerram, D. A. (2017). Mechanisms of overburden deformation associated with the emplacement of the Tulipan sill, mid-Norwegian margin. *Interpretation, 5*(3), SK23-SK38. https://doi.org/10.1190/INT-2016-0155.1

Schofield, N. J., Brown, D. J., Magee, C., & Stevenson, C. T. (2012). Sill morphology and comparison of brittle and non-brittle emplacement mechanisms. *Journal of the Geological Society of London, 169*(2), 127-141. https://doi.org/10.1144/0016-76492011-078

Schofield, N., Alsop, I., Warren, J., Underhill, J. R., Lehné, R., Beer, W., & Lukas, V. (2014). Mobilizing salt: Magma-salt interactions. *Geology*, G35406. 35401. https://doi.org/10.1130/G35406.1

Schofield, N., Holford, S., Millett, J., Brown, D., Jolley, D., Passey, S. R., . . . Stevenson, C. (2017). Regional magma plumbing and emplacement mechanisms of the Faroe-Shetland Sill Complex: implications for magma transport and petroleum systems within sedimentary basins. *Basin Research, 29*(1), 41-63. https://doi.org/10.1111/bre.12164

Schutter, S. R. (2003). Hydrocarbon occurrence and exploration in and around igneous rocks. *Geological Society, London, Special Publications, 214*(1), 7-33. https://doi.org/10.1144/GSL.SP.2003.214.01.02

Skogly, O. (1998). *Seismic characterization and emplacement of intrusives in the Vøring Basin.* (M.Sc. Thesis), University of Oslo.

Smallwood, J. R., & Maresh, J. (2002). The properties, morphology and distribution of igneous sills: modelling, borehole data and 3D seismic from the Faroe-Shetland area. In D. W. Jolley & B. R. Bell (Eds.), *The North Atlantic Igneous Province: Stratigraphy, tectonic, Volcanic and Magmatic Processes* (Vol. 197, pp. 271-306): Geological Society, London, Special Publications. https://doi.org/10.1144/GSL.SP.2002.197.01.11

Sparks, R., Biggs, J., & Neuberg, J. (2012). Monitoring volcanoes. *Science, 335*(6074), 1310-1311. https://doi.org/10.1126/science.1219485

Stearns, D. W. (1978). Faulting and forced folding in the Rocky Mountains foreland. *Geological Society of America Memoirs, 151*, 1-38. https://doi.org/10.1130/MEM151-p1

Sturkell, E., Einarsson, P., Sigmundsson, F., Geirsson, H., Ólafsson, H., Pedersen, R., . . . Stefánsson, R. (2006). Volcano geodesy and magma dynamics in Iceland. *Journal of Volcanology and Geothermal Research, 150*(1-3), 14-34. https://doi.org/10.1016/j.jvolgeores.2005.07.010

Timm, C., Hoernle, K., Werner, R., Hauff, F., van den Bogaard, P., White, J., . . . Garbe-Schönberg, D. (2010). Temporal and geochemical evolution of the Cenozoic intraplate volcanism of Zealandia. *Earth-Science Reviews, 98*(1), 38-64. https://doi.org/10.1016/j.earscirev.2009.10.002

Trude, J., Cartwright, J., Davies, R. J., & Smallwood, J. R. (2003). New technique for dating igneous sills. *Geology, 31*, 4. https://doi.org/10.1130/G19559.1

Uruski, C. I. (2010). New Zealand's deepwater frontier. *Marine and petroleum geology, 27*(9), 2005-2026. https://doi.org/10.1016/j.marpetgeo.2010.05.010

van Wyk de Vries, B., Márquez, A., Herrera, R., Bruña, J. G., Llanes, P., & Delcamp, A. (2014). Craters of elevation revisited: forced-folds, bulging and uplift of volcanoes. *Bulletin of Volcanology*, *76*(11), 1-20. https://doi.org/10.1007/s00445-014-0875-x

Walker, R., Healy, D., Kawanzaruwa, T., Wright, K., England, R., McCaffrey, K., . . . Blenkinsop, T. (2017). Igneous sills as a record of horizontal shortening: The San Rafael subvolcanic field, Utah. *Geological Society of America Bulletin*, B31671. 31671. https://doi.org/10.1130/B31671.1

Figure 1

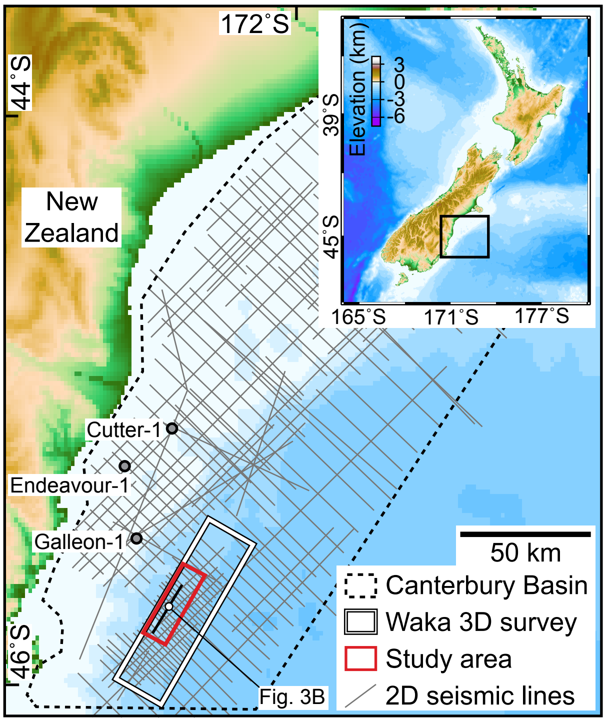
172˚S
44˚S
46˚S
New Zealand
Cutter-1
Endeavour-1
Galleon-1
Fig. 3B
Elevation (km)
3
0
-3
-6
39˚S
45˚S
165˚S
171˚S
177˚S
50 km
Canterbury Basin
Waka 3D survey
Study area
2D seismic lines

Figure 2

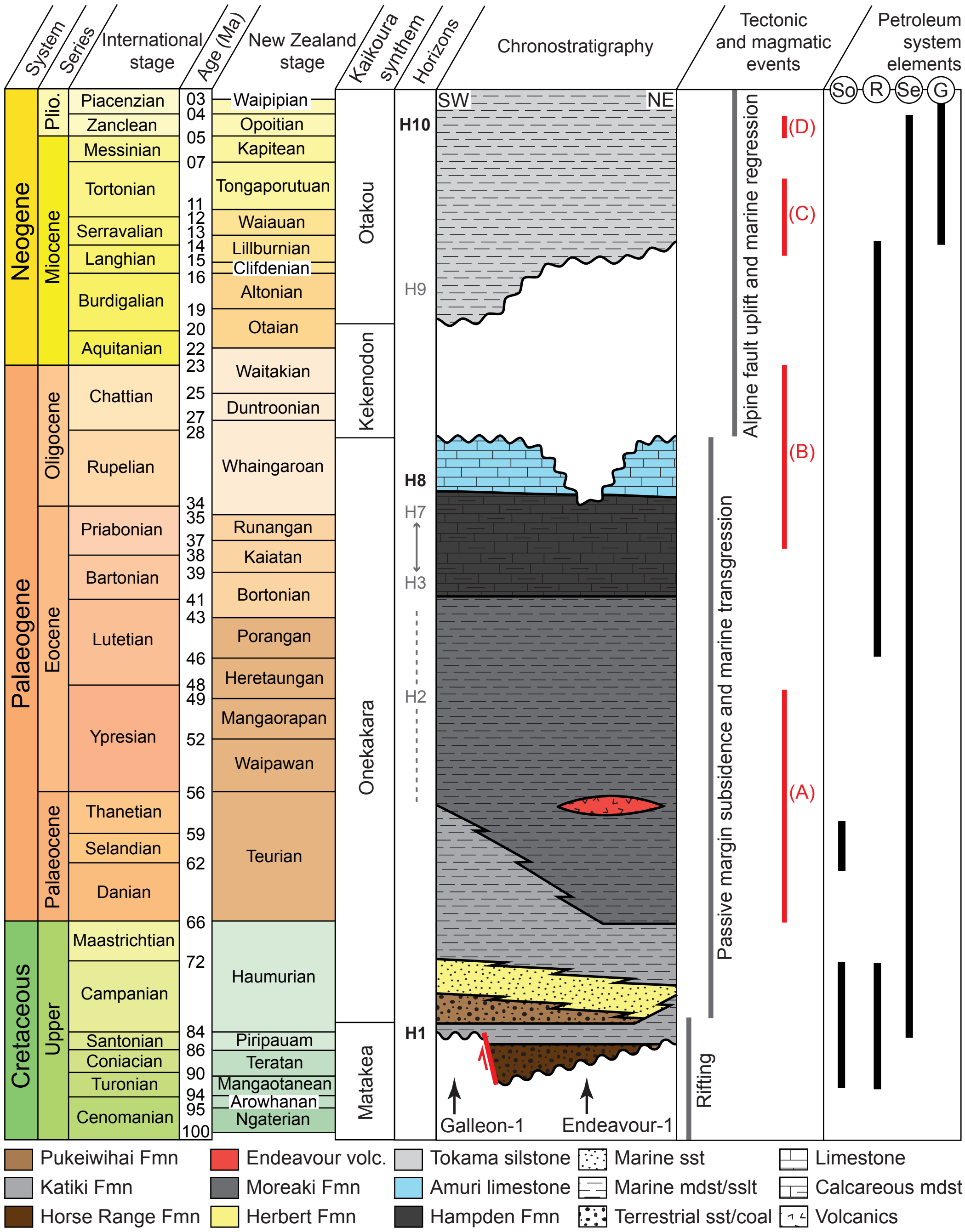

System
Series
International stage
Age (Ma)
New Zealand stage
Kaikoura synthem
Horizons
Chronostratigraphy
Tectonic and magmatic events
Petroleum system elements
So
R
Se
G
Neogene
Palaeogene
Cretaceous
Plio.
Miocene
Oligocene
Eocene
Palaeocene
Upper
Piacenzian
Zanclean
Messinian
Tortonian
Serravalian
Langhian
Burdigalian
Aquitanian
Chattian
Rupelian
Priabonian
Bartonian
Lutetian
Ypresian
Thanetian
Selandian
Danian
Maastrichtian
Campanian
Santonian
Coniacian
Turonian
Cenomanian
03
04
05
07
11
12
13
14
15
16
19
20
22
23
25
27
28
34
35
37
38
39
41
43
46
48
49
52
56
59
62
66
72
84
86
90
94
95
100
Waipipian
Opoitian
Kapitean
Tongaporutuan
Waiauan
Lillburnian
Clifdenian
Altonian
Otaian
Waitakian
Duntroonian
Whaingaroan
Runangan
Kaiatan
Bortonian
Porangan
Heretaungan
Mangaorapan
Waipawan
Teurian
Haumurian
Piripauam
Teratan
Mangaotanean
Arowhanan
Ngaterian
Otakou
Kekenodon
Onekakara
Matakea
H10
H9
H8
H7
H3
H2
H1
SW
NE
Galleon-1
Endeavour-1
Alpine fault uplift and marine regression
Passive margin subsidence and marine transgression
Rifting
(D)
(C)
(B)
(A)
Pukeiwihai Fmn
Katiki Fmn
Horse Range Fmn
Endeavour volc.
Moreaki Fmn
Herbert Fmn
Tokama silstone
Amuri limestone
Hampden Fmn
Marine sst
Marine mdst/sslt
Terrestrial sst/coal
Limestone
Calcareous mdst
Volcanics

Figure 3

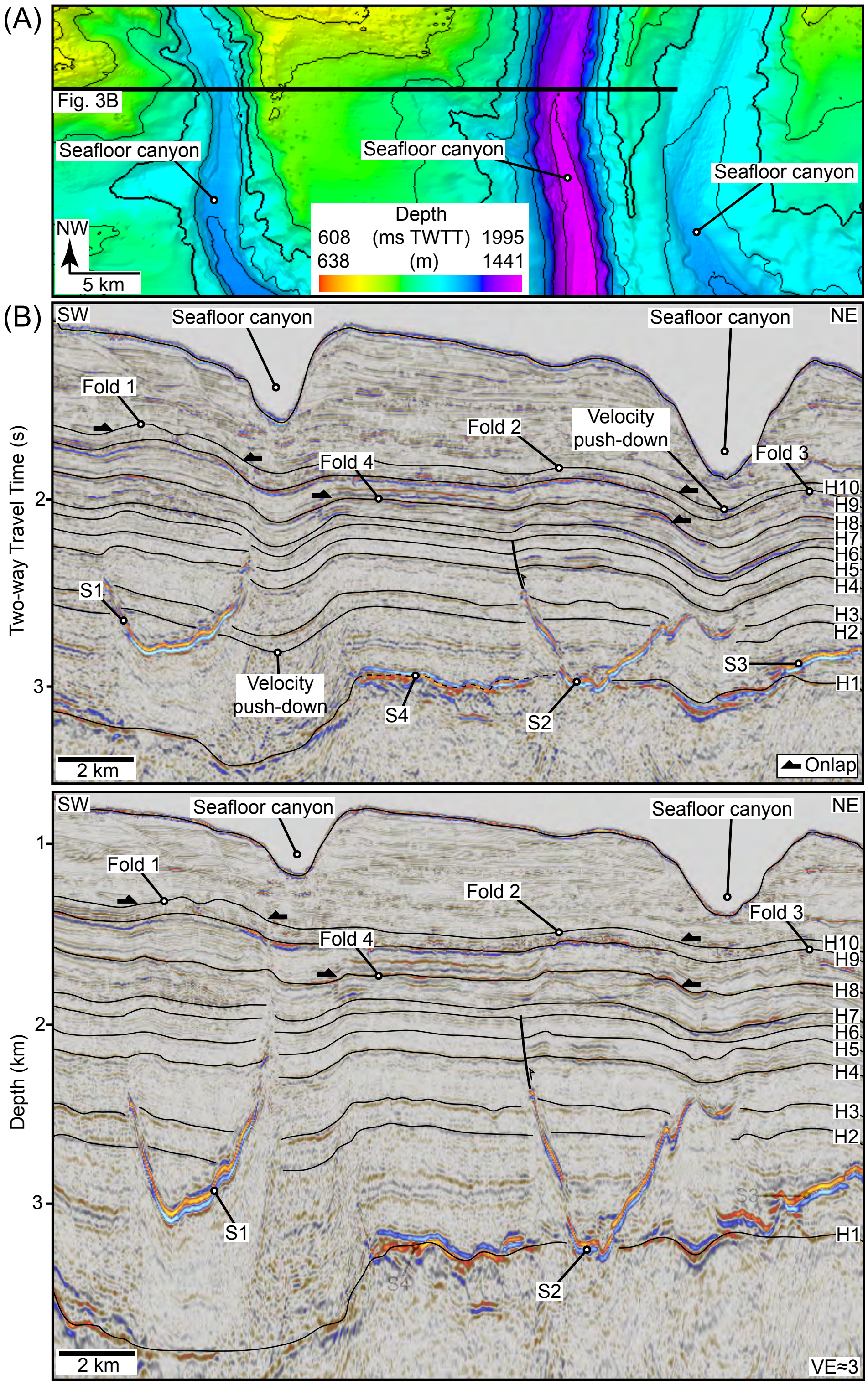

(A)
Fig. 3B
Seafloor canyon
Seafloor canyon
Seafloor canyon
NW
5 km
Depth
608 (ms TWTT) 1995
638 (m) 1441
(B)
SW
NE
Seafloor canyon
Seafloor canyon
Fold 1
Fold 2
Fold 3
Fold 4
Velocity push-down
Velocity push-down
Two-way Travel Time (s)
2
3
S1
S2
S3
S4
H10
H9
H8
H7
H6
H5
H4
H3
H2
H1
2 km
Onlap
SW
NE
Seafloor canyon
Seafloor canyon
Fold 1
Fold 2
Fold 3
Fold 4
Depth (km)
1
2
3
S1
S2
S3
S4
H10
H9
H8
H7
H6
H5
H4
H3
H2
H1
2 km
VE≈3

Figure 4

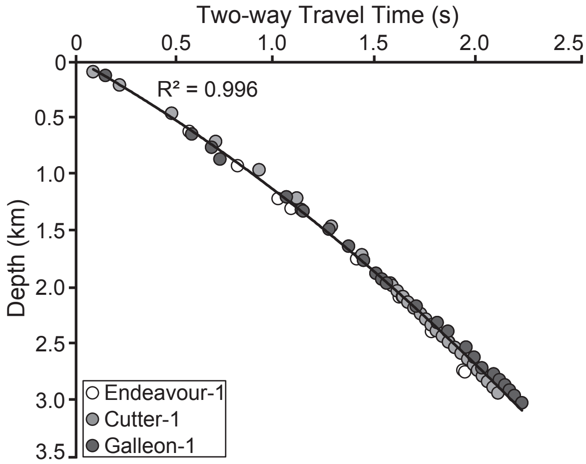
Two-way Travel Time (s)
0
0.5
1.0
1.5
2.0
2.5
Depth (km)
0
0.5
1.0
1.5
2.0
2.5
3.0
3.5
R² = 0.996
Endeavour-1
Cutter-1
Galleon-1

Figure 5

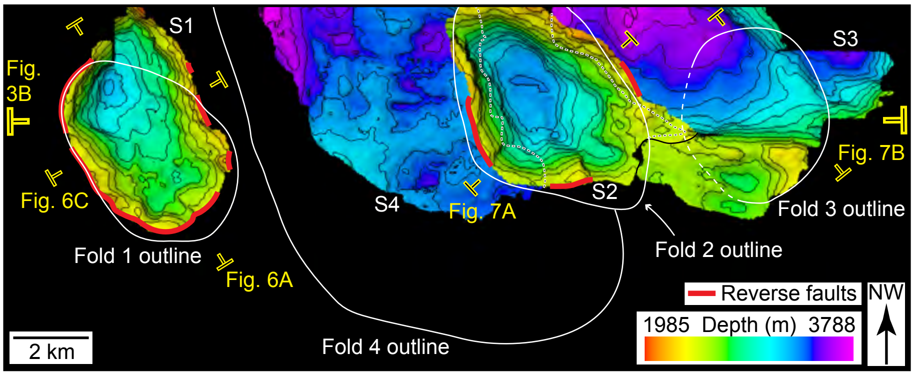
S1
Fig. 3B
Fig. 6C
Fold 1 outline
Fig. 6A
S4
Fig. 7A
S2
Fold 2 outline
S3
Fig. 7B
Fold 3 outline
Fold 4 outline
Reverse faults
1985 Depth (m) 3788
NW
2 km

Figure 6

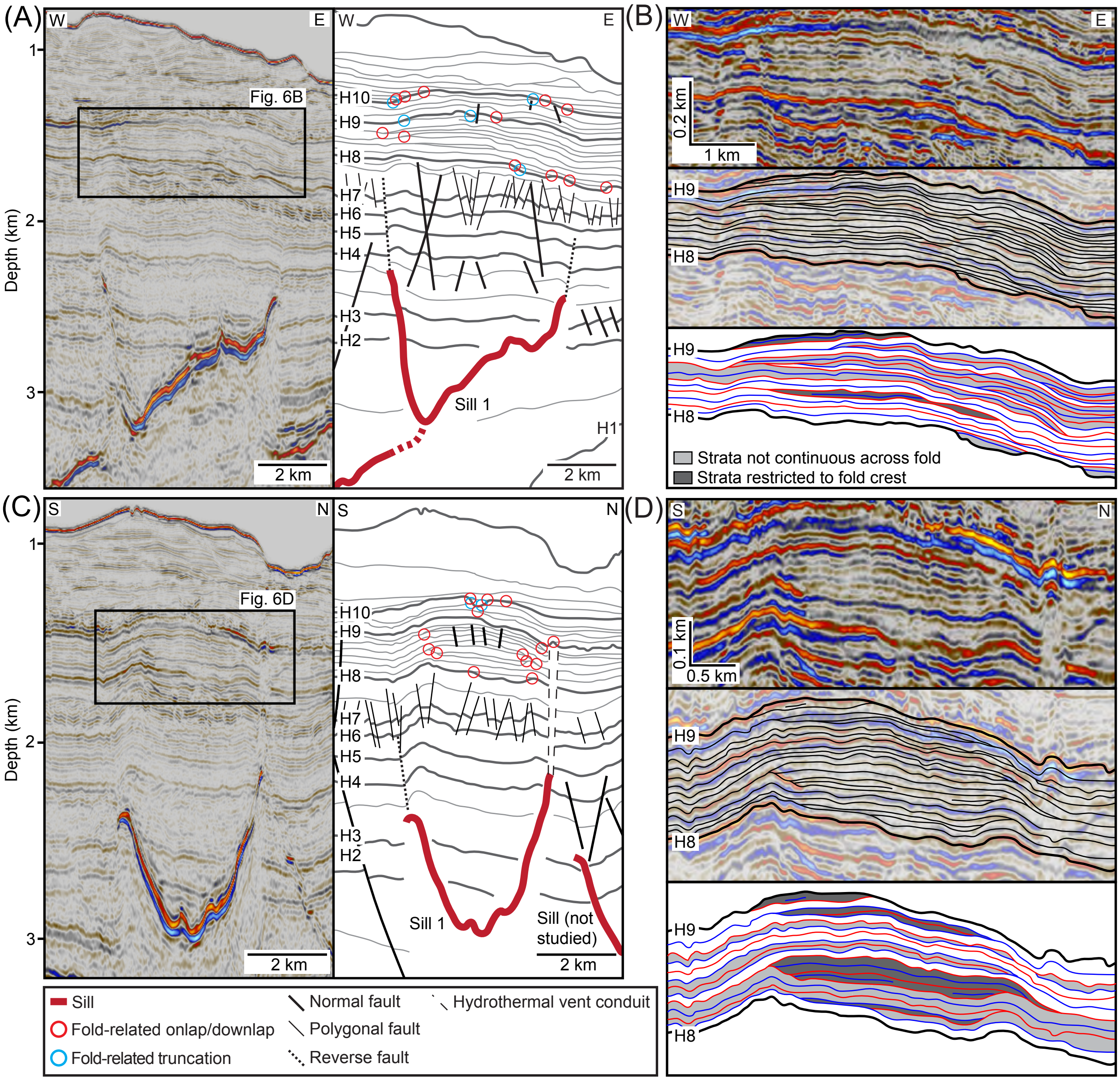

(A)
W
E
Fig. 6B
Depth (km)
1
2
3
2 km
W
E
H10
H9
H8
H7
H6
H5
H4
H3
H2
Sill 1
H1
2 km
(B)
W
E
0.2 km
1 km
H9
H8
H9
H8
Strata not continuous across fold
Strata restricted to fold crest
(C)
S
N
Fig. 6D
Depth (km)
1
2
3
2 km
S
N
H10
H9
H8
H7
H6
H5
H4
H3
H2
Sill 1
Sill (not studied)
2 km
(D)
S
N
0.1 km
0.5 km
H9
H8
H9
H8
Sill
Fold-related onlap/downlap
Fold-related truncation
Normal fault
Polygonal fault
Reverse fault
Hydrothermal vent conduit

Figure 7

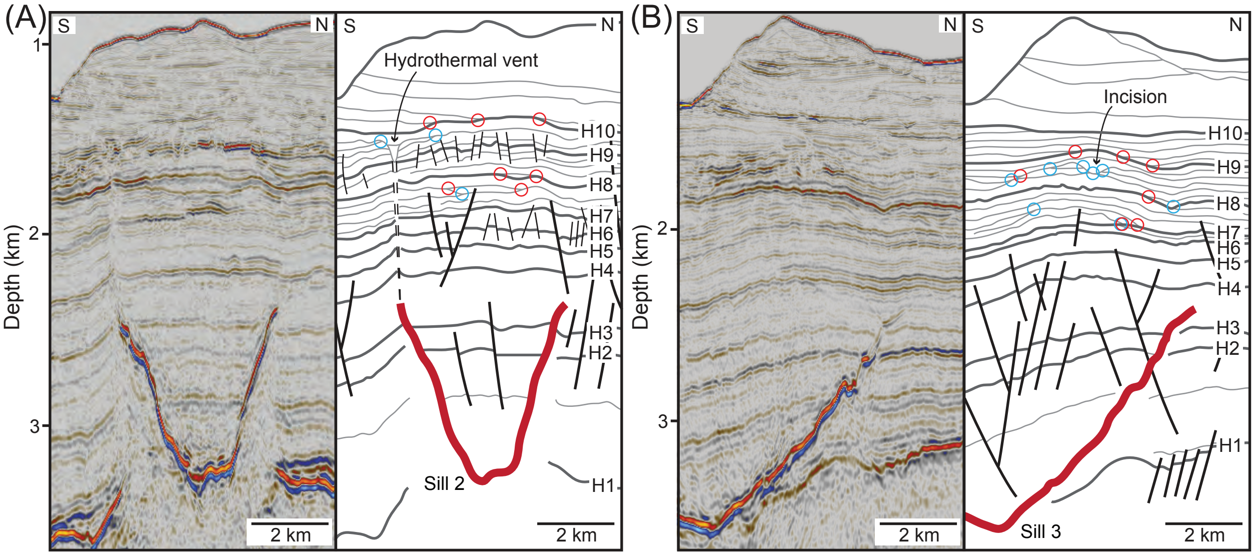

(A)
S
N
1
2
3
Depth (km)
2 km
S
N
Hydrothermal vent
H10
H9
H8
H7
H6
H5
H4
H3
H2
H1
Sill 2
2 km
(B)
S
N
2
3
Depth (km)
2 km
S
N
Incision
H10
H9
H8
H7
H6
H5
H4
H3
H2
H1
Sill 3
2 km

Figure 8

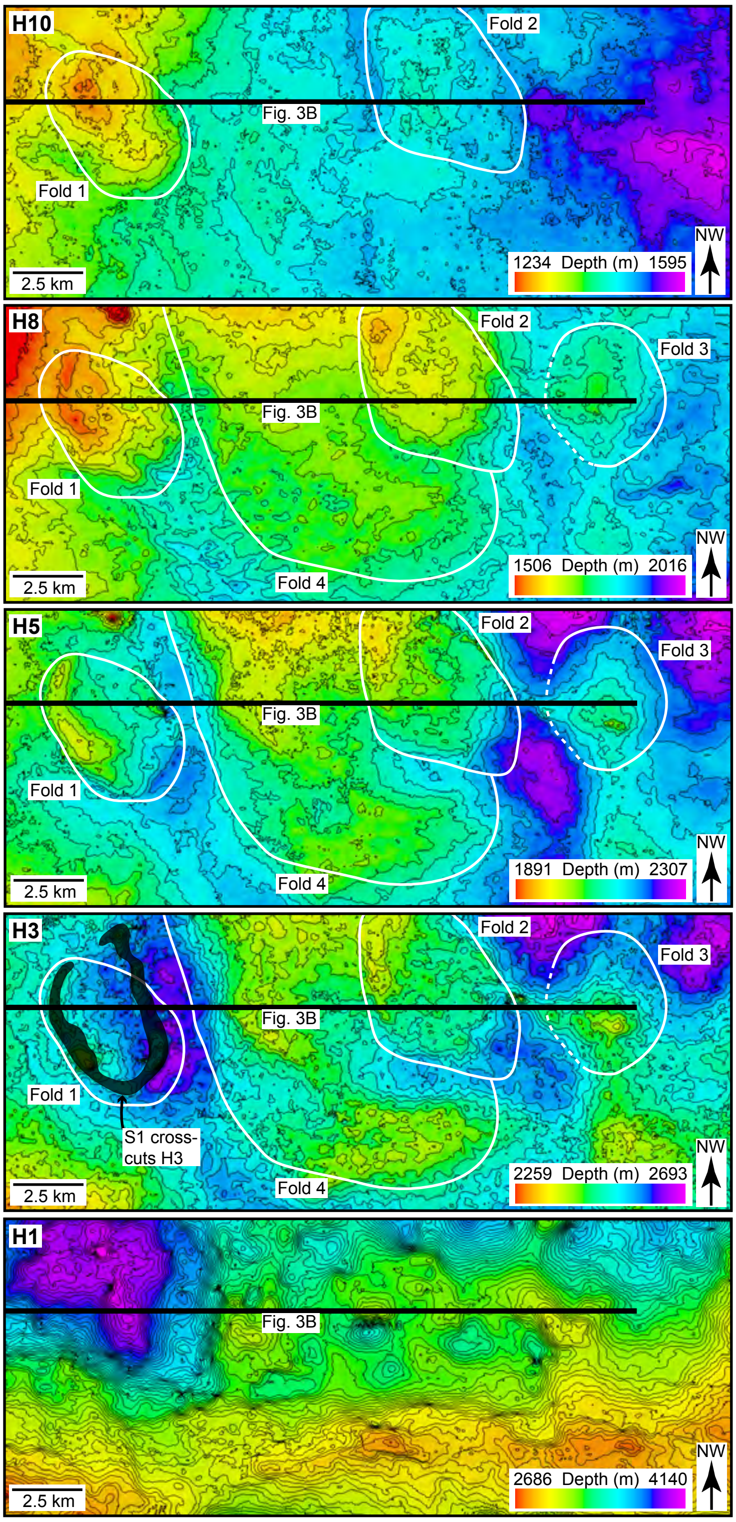
H10
Fold 2
Fold 1
Fig. 3B
2.5 km
1234 Depth (m) 1595
NW
H8
Fold 2
Fold 3
Fold 1
Fold 4
Fig. 3B
2.5 km
1506 Depth (m) 2016
NW
H5
Fold 2
Fold 3
Fold 1
Fold 4
Fig. 3B
2.5 km
1891 Depth (m) 2307
NW
H3
Fold 2
Fold 3
Fold 1
Fold 4
Fig. 3B
S1 cross-cuts H3
2.5 km
2259 Depth (m) 2693
NW
H1
Fig. 3B
2.5 km
2686 Depth (m) 4140
NW

Figure 9

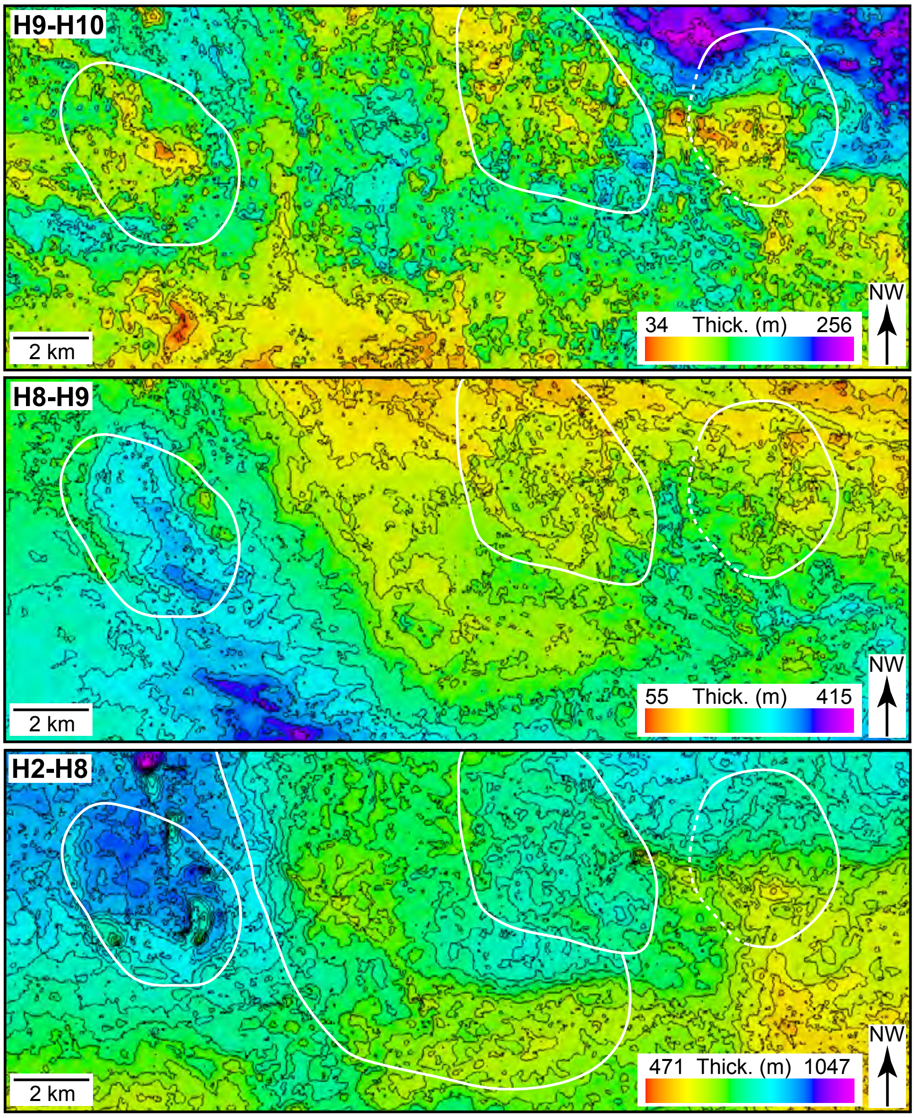
H9-H10
2 km
34 Thick. (m) 256
NW
H8-H9
2 km
55 Thick. (m) 415
NW
H2-H8
2 km
471 Thick. (m) 1047
NW

Figure 10

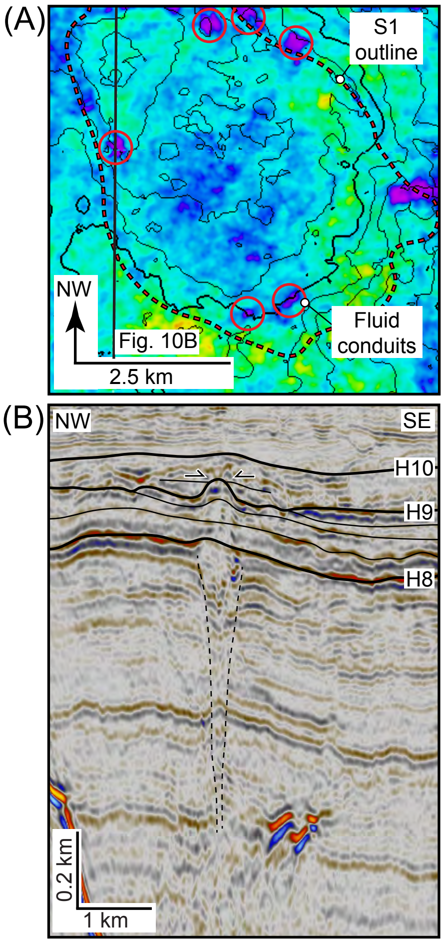

(A)
S1
outline
NW
Fig. 10B
2.5 km
Fluid
conduits
(B)
NW
SE
H10
H9
H8
0.2 km
1 km

Figure 11

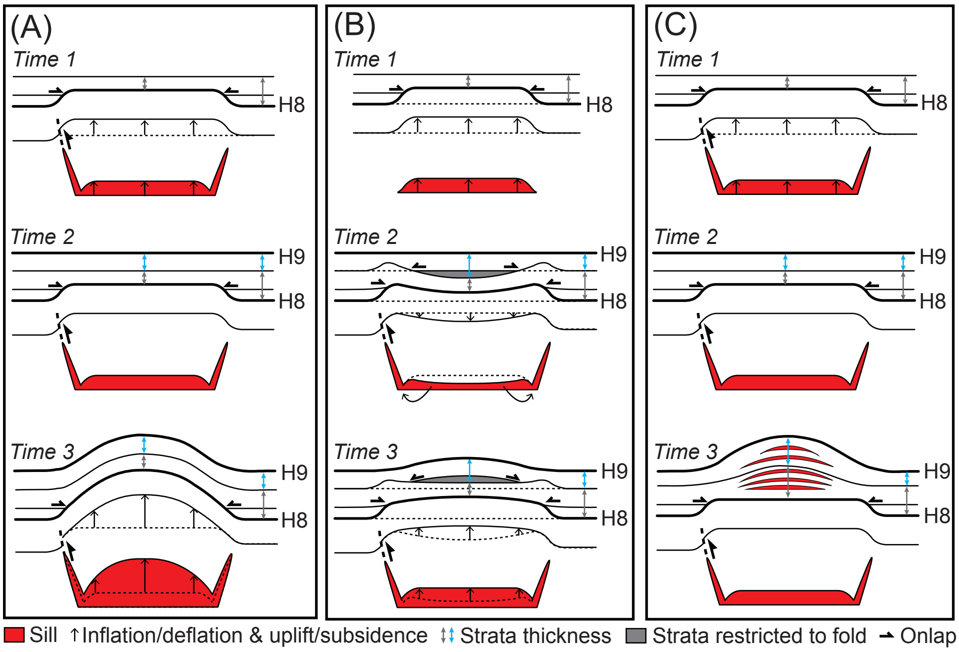

(A)
Time 1
H8
Time 2
H9
H8
Time 3
H9
H8
(B)
Time 1
H8
Time 2
H9
H8
Time 3
H9
H8
(C)
Time 1
H8
Time 2
H9
H8
Time 3
H9
H8
Sill
Inflation/deflation & uplift/subsidence
Strata thickness
Strata restricted to fold
Onlap